# Phase-controlled stair-step decay of autoionizing radial wave packets

S. N. Pisharody and R. R. Jones
*Department of Physics, University of Virginia, Charlottesville, Virginia 22904*
(Received 6 October 2001; published 27 February 2002)

The time-dependent survival probabilities of autoionizing $4pNd$ wave packets in calcium have been measured. Femtosecond laser pulses induce sequential isolated-core excitations of singly excited $4sNd$ radial wave packets to create and probe the nonstationary doubly excited states. Stair step rather than exponential decay of the wave packets is observed. Moreover, we show that the autoionization lifetime can be varied by a factor of five by adjusting the relative phases of the constituent eigenstates in the packet. The stair-step decay structure and its dependence on the wave packet phase is interpreted using an intuitive time-domain picture. The experimental results are in excellent agreement with a *K*-matrix based, 28-channel quantum-defect theory calculation as well as with an approximate two-channel formulation.

DOI: 10.1103/PhysRevA.65.033418 PACS number(s): 32.80.Rm, 32.80.Dz, 32.80.Qk

## I. INTRODUCTION

The use of coherent laser radiation to modify and control chemical reaction rates and pathways is a long-standing dream in chemical physics and physical chemistry [1]. Yet in spite of enormous advances in laser and optical technology and the development of new theoretical methods, experimental demonstrations of quantum-controlled chemistry are still relatively few in number [2,3]. In large part, this is due to the extreme complexity of the molecular systems of interest. Not surprisingly, a number of investigators have considered relatively simple systems for proof-of-principle tests of laser control schemes [4–7]. Doubly excited Rydberg atoms are particularly interesting in this regard for several reasons [8–13]. First, configuration interaction in two-electron atoms is analogous to the coupling between rotational, vibrational, and electronic modes in molecules. Because each electron moves in a noncentral potential, energy and angular momentum are not conserved for each electron individually. Instead, at energies above the first ionization limit, dielectronic eigenstates with well-defined total angular momentum are linear combinations of bound and continuum configurations with different angular and principal quantum numbers for the respective electrons. In the time domain, two valence electrons, each with well-defined energy and angular momentum, coherently scatter and exchange energy and angular momentum [14]. The collision rate and number of dielectronic modes that are accessible during each collision are readily tuned by increasing the total energy and/or angular momentum of the system. Second, sophisticated methods for creating and viewing singly excited Rydberg wave packets with specific dynamical properties have been demonstrated [15–18]. This fact, coupled with the wealth of spectroscopic information that is available for two-electron atoms suggests that one might be able to intuitively control time-dependent configuration interaction and the byproducts of autoionization by designing the appropriate doubly excited wave packets. Third, well-established numerical methods, involving multichannel quantum-defect theory (MQDT) and *ab initio K* matrix theory, enable full quantum simulations of absorption spectra and dynamics in two-electron atoms, particularly at energies well below the second ionization limit [19–26]. Comparison of experimental results with exact theoretical analyses allows one to unambiguously determine whether limited control efficiencies should be attributed to the physics that governs the system, or to experimental errors and limitations [13]. Lastly, in the presence of visible and near-visible laser radiation, the alkaline earths, Mg, Ca, Sr, and Ba are excellent approximations of two-electron atoms. These elements are easy to handle and are readily vaporized in vacuum to form atomic beams.

In recent years, a significant number of investigators have employed ultrafast laser pulses to examine doubly excited two-electron atoms [10–14,27–29]. However, most of these studies have used time-domain spectroscopies to probe naturally occurring time-dependent configuration interaction and autoionization. To the best of our knowledge, only a handful of experiments have used laser light to alter the dielectronic dynamics, either through direct atom/field coupling [8,10,11] or through the creation of specific doubly excited wave packets that are predisposed to evolve in particular ways [12,13]. Here we consider the decay of tailored autoionizing radial Rydberg wave packets. We find that the time-dependent decay of such wave packets can be remarkably nonexponential. Moreover, the autoionization lifetime of the doubly excited atom can be changed by a factor of 5 or more by altering the relative phases of the constituent eigenstates in the wave packet.

In the following section the experimental procedure and results are presented. Next, we formulate a semiclassical model that qualitatively explains the observed nonexponential decay of the wave packets as well as the phase dependence of the autoionization lifetimes. An approximate two-channel QDT that uses a single, adjustable, decay-rate parameter is shown to quantitatively reproduce the experimental data. However, we note a discrepancy between the value of the decay-rate parameter required to fit our current data as compared to that used to reproduce the nonexponential decay spectra previously observed for autoionizing ''shock wave packets'' [30]. Lastly the result of a 28-channel

 ©2002 The American Physical Society

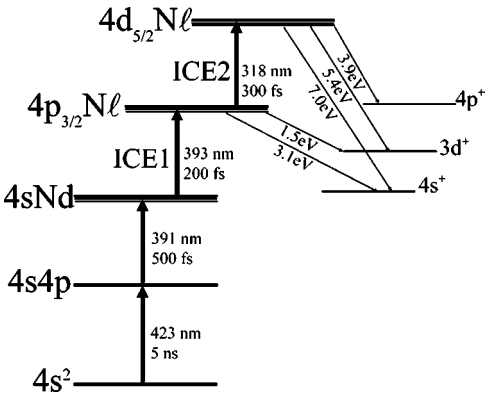


FIG. 1. Schematic energy-level diagram indicating the wavelength and duration of the excitation and probe laser beams and the energies of the electrons emitted from the laser-excited autoionizing states.

QDT simulation using *ab initio K*-matrix parameters is presented. While the theoretical curves are in excellent agreement with the *current* data, there is a small, but significant, difference between the measured and numerical shock wave packet decay curves.

## II. EXPERIMENTAL PROCEDURE

The experimental procedure is nearly identical to that used previously to measure the nonexponential decay of autoionizing shock wave packets [30]. Briefly, a thermal beam of ground-state Ca atoms is exposed to four consecutive laser pulses (see Fig. 1). The first laser pulse (423 nm, 5 nsec) promotes atoms in the $4s^2\,{}^1S_0$ ground state into an intermediate $4s4p\,{}^1P_1$ state. The second pulse (392 nm, 500 fsec) coherently transfers electron population from the $4s4p$ level to a superposition of $4snd\,{}^1D_2$ eigenstates. This superposition state, or wave packet, is characterized by an average principal quantum number $N$ and evolves for a time, $T_1$, before undergoing a sudden isolated core excitation (ICE) [31] $4sNd$-$4p_{3/2}N\ell$. The ICE is initiated by a third laser pulse, hereafter referred to as ICE1 (393 nm, 200 fsec). The doubly excited $4p_{3/2}N\ell$ atoms decay by ejection of electrons with energies of 1.5 eV or 3.1 eV corresponding to $3d\epsilon\ell$ and $4s\epsilon\ell$ continua, respectively. The time-dependent autoionization decay of these atoms is probed by initiating a second ICE at some time $T_2$ following the first ICE. The probe ICE is accomplished using a fourth laser pulse (ICE2, 318 nm, 300 fsec) that further excites a fraction of the atoms remaining in $4p_{3/2}N\ell$ configuration to a superposition of $4d_{5/2}N\ell$ states. As shown in Fig. 1, atoms in $4d_{5/2}N\ell$ states decay into a number of final ionic states via the emission of electrons with energies of 3.9, 5.4, and 7.0 eV. Such high-energy electrons are only produced during autoionization of $4d_{5/2}N\ell$ atoms. Therefore, the number of high-energy electrons generated on a given laser shot is directly proportional to the probability that the atom was in the $4p_{3/2}N\ell$ configuration at the instant the atoms were exposed to the fourth laser pulse (ICE2). By detecting the number of high-energy electrons as a continuous function of the delay $T_2$ we measure the time-dependent decay of the $4p_{3/2}N\ell$ wave packet.

The three subpicosecond laser pulses used in the experiment are derived from a single 120 fsec, 787 nm laser pulse that is produced by an amplified, self-mode-locked Ti:Sapphire oscillator [30]. The second laser pulse, which is responsible for the creation of the singly-excited $4snd$ wave packet, is produced by spectrally filtering and then frequency doubling a fraction of the 787 nm beam [18]. The average binding energy and number of eigenstates in the $4snd$ wave packet are selectable by modifying the central frequency and width of the spectral filtering aperture [32]. The third laser pulse ICE1 is obtained by frequency doubling an unfiltered portion of the 787 nm pulse. The fourth laser pulse ICE2 is created by mixing the 534 nm output of an optical parametric amplifier (OPA) with the 787 nm Ti:sapphire beam. The OPA itself is pumped by a 200 fsec, 393 nm frequency-doubled Ti:sapphire pulse. The lasers fire at a 15 Hz repetition rate and are all linearly polarized in the vertical direction.

Electrons produced via autoionization of the laser-excited atoms pass through a time-of-flight spectrometer and are collected with a dual microchannel plate (MCP) detector. High-energy electrons ($>3.5$ eV) produced during the decay of the $4dnd$ atoms are easily distinguished from the low-energy electrons (3.1 and 1.5 eV) that are the result of autoionization from the $4pnd$ levels. The eigenstate composition of the $4snd$ wave packet is measured using state-selective field ionization (SSFI) of atoms remaining in bound Rydberg states following the ICE pulses [21]. Typical SSFI traces for $N=35$ and $N=40$ wave packets are shown in Fig. 2.

## III. EXPERIMENTAL RESULTS

We have studied in detail, the decay of $4pNd$ radial wave packets with average principal quantum number $N=35$ and $N=40$. Considering that the $4snd$ quantum defect at these energies is approximately 1.2, the wave packets have classical Kepler periods $\tau_K=5.9$ psec and 8.9 psec, respectively. Figure 3 shows the survival probability of $4pNd$, $N=40$ autoionizing wave packets as a function of the time delay $T_2$ between the excitation of the $4pNd$ wave packet and the appearance of the ICE2 probe. From bottom to top, the curves in Fig. 3 are the survival probabilities for $N=40$ wave packets created at increasing values of $T_1$, at approximately constant intervals. The sequence of curves has several notable features. First, none of the curves appear to be exponential. Instead, in all cases, the survival probability remains nearly constant and then decreases by approximately 85% over a 1.5 psec time interval. Close inspection indicates a second plateau region and 85% drop following the first step of the decay. This second step is more apparent in Fig. 5. Second, the duration of the initial plateau changes dramatically, and nonmonotonically with increasing $T_1$. As $T_1$ is increased from zero to $\tau_K$ the duration of the plateau decreases linearly with $T_1$. The lifetime of the autoionizing wave packet changes by approximately a factor of 5 over the interval $0<T_1<\tau_K$. At a delay just greater than $\tau_K$, the plateau width suddenly increases, returning to its value at

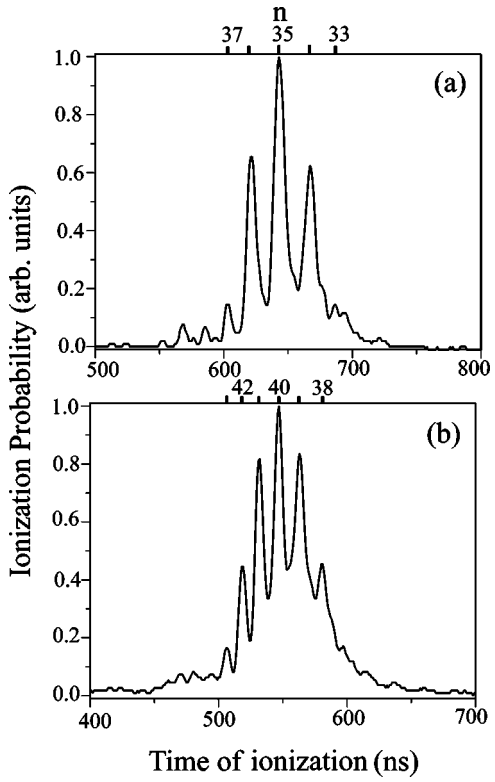


FIG. 2. State-selective field ionization (SSFI) electron spectrum indicating the eigenstate distribution in the (a) $N=35$ and (b) $N=40$ wave packets that are investigated.

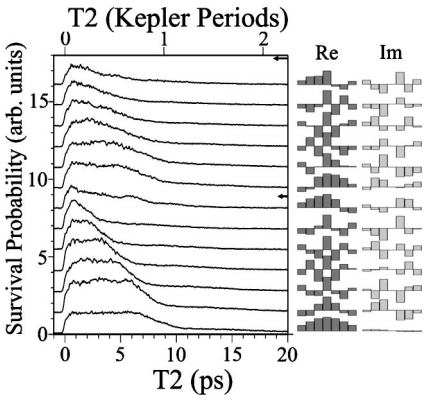


FIG. 3. Survival probability of the autoionizing $4pNd$, $N=40$ wave packet as a function of the ICE2 probe delay, $T_2$. The vertical offset of each trace is proportional to the delay $T_1$ of ICE1 after the creation of the $4snd$ radial wave packet. The upper scale shows the delay $T_2$ in units of the Kepler period of the wave packet. From top to bottom, the two arrows on the right-hand side of the main figure mark delays of $T_1=2\tau_K$ and $T_1=\tau_K$, respectively. The bar graphs on the right-hand side of the main figure indicate the calculated real and imaginary amplitudes of the constituent $4snd$ eigenstates in the wave packet at time delays corresponding to the curves in the main figure. Note that the only difference between the decay curves is the complex phase of the constituent $4snd$ eigenstates at the instant of the $4sNd$-$4pNd$ transition.

$T_1=0$. The pattern repeats again for $\tau_K<T_1<2\tau_K$. Third, the duration of the second probability step is approximately $\tau_K$, independent of $T_1$. These same characteristics are observed in analogous decay curve sequences for $N=35$ wave packets as well.

Assuming the laser pulse that creates the $4sNd$ wave packet appears at time $t=0$, its wave function at later times $T_1$ can be written in terms of the constituent eigenstates, $|4sNd\rangle=\Sigma_n C_n|4snd\rangle e^{-iE_nT_1}$ (a.u.). Here $E_n=-1/2n^2$ is the energy of the $4snd$ Rydberg level. To a good approximation in this experiment, the eigenstate amplitudes $C_n$ are real, and the time-independent probability that the electron is in a particular $|4snd\rangle$ state, as determined by the SSFI measurements, is $C_n^2$. With increasing $T_1$, the changes in the bound wave packet cause the strikingly different decay curves shown in Fig. 3. These differences are due entirely to the evolution of the complex phase $e^{-iE_nT_1}$ of each eigenstate. Therefore, in the experiment, we probe the decay of a class of doubly excited wave packets that differ only in the complex phase of the constituent eigenstates at the instant of the ICE. Such phase-shaped wave packets may also be produced, albeit with significantly higher experimental difficulty, by manipulating the spectral-phase profile of the laser pulse that produces the wave packet [17,33]. Therefore, it seems appropriate to consider the observed modification of autoionization lifetimes in the context of experiments exploring phase control of quantum dynamics.

The insets of Fig. 3 show the calculated real and imaginary parts of the $4sNd$, $N=40$, eigenstate amplitudes at delays corresponding to the respective survival probability curves. Unfortunately, inspection of the insets provides little if any insight as to the source of the stair-step decay and the significant variation in the autoionization lifetimes. Most notable is the situation near $T_1=\tau_K$ where a modest change in the real and imaginary amplitude distribution results in a change in the observed lifetime from approximately 2 to 7 psec.

Alternatively, we present a semiclassical picture that provides a qualitatively complete description of the physics responsible for the intriguing form of the observed decay curves. To a first approximation, the two valence electrons in the $4pNd$ doubly excited atoms can be considered to be independent particles. In classical terms, the Rydberg electron moves in an extended orbit in the potential of a singly charged ionic core. The other electron is tightly bound to a doubly charged ion. Autoionization occurs when the two electrons collide and exchange energy and angular momentum via their mutual Coulomb repulsion. Since the ionic $4p$ electron is confined to a small volume very near the nucleus, these collisions can only occur at times when the Rydberg electron is also near the ionic core. Quantum mechanically, at any instant, the autoionization rate is directly proportional to the probability for finding the Rydberg electron near the nucleus at that time. Since the Rydberg electron is in a nonstationary state, changes in the autoionization rate reflect the time-dependent probability for finding the electron near the ionic core. Figure 4 shows the calculated radial probability

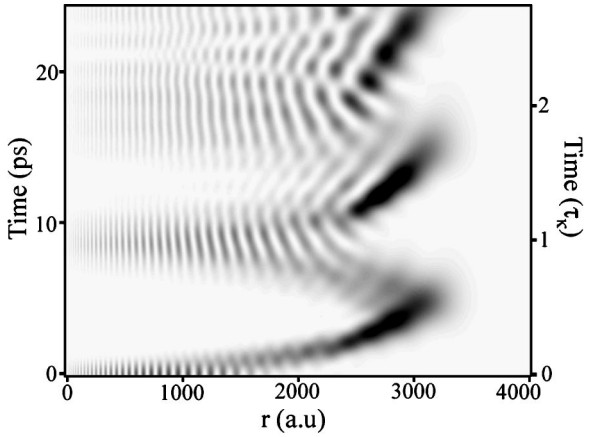


FIG. 4. Calculated time-dependent radial probability distribution for a $4sNd$, $N=40$ wave packet. Dark indicates high probability. The wave packet spends most of its time near the classical outer turning point in the Coulomb potential. It moves rapidly past the ionic core once every Kepler period.

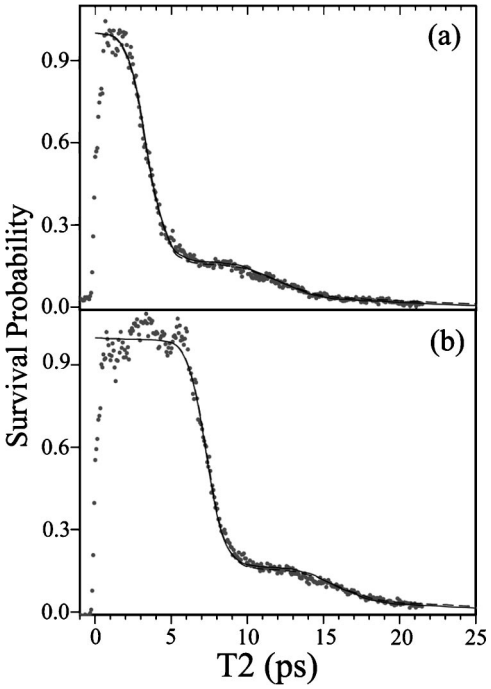


FIG. 5. Measured survival probability for the autoionizing $4pNd$, $N=40$ wave packet at ICE1 time delays of (a) $T_1=1.4$ psec and (b) $T_1=5.4$ psec. The solid and dashed curves are the results of the two-channel and 28-channel QDT calculations, respectively. As discussed in the text, the 28-channel simulation has no adjustable parameters, and a scaled decay rate $\gamma=0.29$ is used in the two-channel fit.

distribution for a $4sNd$, $N=40$ wave packet as a function of delay following its creation. Immediately following its excitation from the tightly bound $4s4p$ intermediate state, the wave packet is localized near the nucleus, but is expanding radially. The packet moves outward, reflects from the Coulomb potential at a radius of approximately $2N^2 \approx 3200$ a.u., and returns to the nucleus. Dispersion due to the nonequally spaced energies of the contributing eigenstates leads to collapse and revivals of the wave packet motion as it evolves in time. [15]

Armed with this intuitive picture, we can qualitatively explain the data shown in Fig. 3. If ICE1 appears just following the launch of the wave packet ($T_1 \approx 0$), there is essentially zero probability of finding the electron near the nucleus until one Kepler period later. Therefore, as observed, the survival probability remains constant for a time $T_2=\tau_K$. As the wave packet approaches the nucleus, the autoionization rate increases suddenly and dramatically, producing a rapid decrease in the $4pNd$ survival probability. A second plateau in the probability occurs as the wave packet moves out and back during the second Kepler period. If, instead, the core electron is excited when $T_1=\tau_K/2$, the Rydberg wave packet is near the outer turning point of its motion during ICE1. Consequently, it requires a time $T_2=\tau_K/2$ to return to the nucleus, and the first plateau in the decay curve has a duration $\tau_K/2$. After passing the nucleus the wave packet requires a full Kepler period to return, which defines the duration of the second plateau. For ICE1 delays just less than $\tau_K$, the wave packet crashes into the ionic core almost immediately, resulting in the minimum autoionization lifetime. If $T_1$ is increased slightly beyond one Kepler period, the wave packet is on its way out and the plateau extends to its maximum value once again. In all of the decay curves, the duration of the transition between steps reflects the temporal width of the wave packet as it passes the nucleus. In addition, the fractional decrease in probability at each step is proportional to the autoionization rate of the constituent eigenstates in the wave packet. As shown more clearly in Fig. 5, only two distinct steps are observed due to the large autoionization rate of the $4pNd$ states and the broadening of the step transition due to wave packet dispersion.

## IV. TWO-CHANNEL QUANTUM DEFECT THEORY ANALYSIS

Previous measurements of the autoionization decay of shock wave packets in the identical Ca $4pnd$ system are well described using a two-channel QDT analysis [30]. An analogous procedure is used here in an attempt to quantitatively reproduce the observed $4pNd$ radial wave packet decay curves. The model assumes that there are only two relevant final-state channels, one bound and one continuum. At a given delay $T_1$, following the launch of the $4sNd$ wave packet, the energy-dependent transition moment to the $4pnd$ states is [20,34,30]

$$T(W_\nu,T_1) \propto \sum_n C_n e^{-\imath W_n T_1} A(\nu)\Theta(\nu,n), \qquad (1)$$

where $C_n$ is the amplitude of an eigenstate with effective principal quantum number $n^*=n-\delta_i$, $A(\nu)=1/\sin\pi(\nu+\delta_f+\imath\gamma/2)$ is the spectral density in the $4p_{3/2}$ channel and

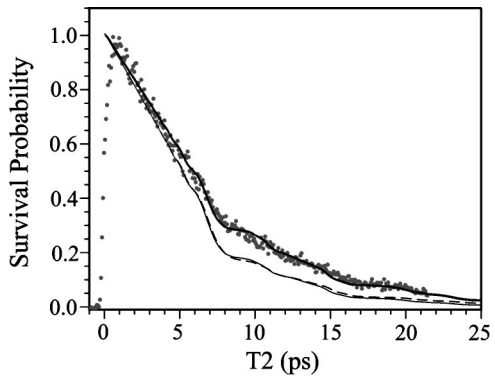


FIG. 6. Measured survival probability for an autoionizing $4pNd$, $N=40$ shock wave packet. The thick solid curve is the result of the two-channel QDT fit with $\gamma=0.21$, while the thin solid line shows the result for $\gamma=0.29$. The dashed curve is the result of the 28-channel QDT calculations as discussed in the text. As shown in Fig. 5, accurate reproduction of the radial wave packet data requires $\gamma=0.29$.

$\Theta(\nu,n)=\sin\pi(\nu-n^*)/W_\nu-W_n$ is the overlap integral for the ICE transition [35]. $W_\nu=-1/2\nu^2$ is the energy of the autoionizing wave packet with respect to the $4p_{3/2}$ ionization limit; $W_n=-1/2n^{*2}$ is the energy of the Rydberg eigenstate with respect to the $4s$ ionization limit; $\delta_i$ and $\delta_f$ are the quantum defects of the initial and final state configurations, $\gamma=n^{*3}\Gamma_n$ is the energy-independent scaled-autoionization rate, and $\Gamma_n$ is the autoionization rate of the $4p_{3/2}nd$ autoionizing level. The time-dependent decay rate is obtained by Fourier transforming the product of the energy-dependent transition moment with the spectral amplitude $F(W)$ of the ICE1 laser pulse,

$$R(t,T_1)=\left|\int dW_\nu e^{-\imath W_\nu t}T(W_\nu,T_1)F(W_{3/2}+W_\nu-W_n)\right|^2, \tag{2}$$

where $W_{3/2}$ is the energy of the $Ca^+4p_{3/2}$ level relative to the $4s$ ionic ground state. The time-dependent autoionization probability is $P(t,T_1)=\int^t R(t',T_1)dt'$, and conservation of probability dictates that the population remaining in the $4pNd$ wave packet at time $t$ is

$$P(t,T_1)=1-\int^t R(t',T_1)dt'. \tag{3}$$

The results of the calculation are uniformly in very good agreement with the data, both for different wave packets and different delays, $T_1$. Typical theoretical curves are shown with data for the $N=40$ wave packet in Fig. 5. Note that the calculation incorporates the measured eigenstate distribution in the $4sNd$ wave packet, the measured frequency spectrum of ICE1, and the known quantum defects for the $4snd$ and $4p_{3/2}nd$ levels [36,37]. The only free parameter that has been adjusted to achieve the agreement shown is the scaled autoionization rate $\gamma$. We find the best agreement between theory and experiment for $\gamma=0.29$. Interestingly, this value is in significant disagreement with the value $\gamma=0.21$ that is required to achieve excellent agreement between measured and calculated shock-wave packet decay curves (see Fig. 6) [30]. Note that the only difference between the shock and radial wave packet experiments is that ICE1 acts on a single $4snd$ eigenstate in the former and on a superposition of $4snd$ eigenstates in the latter. Moreover, since $\gamma$ is a property of the entire $4pnd$ series, its value should be independent of whether or not a single eigenstate or wave packet undergoes the ICE.

After noting the differences in the values of $\gamma$ required to fit the two data sets, we immediately suspected that something in the experimental apparatus or procedure was at the root of the problem. Therefore, the eigenstate and wave packet experiments were repeated under identical conditions, only a few hours apart. The new data sets matched those from the previous experiments perfectly, indicating a real difference between the apparent autoionization rates for the two different wave packets.

Another possible source of the discrepancy between data and theory in the two experiments is the distinction between the quantity that is actually measured and that which is calculated. The numerical simulations provide a prediction for the time-dependent survival probability of atoms excited into the $4pNd$ configuration. In the experiment, the probability that atoms decay from $4dNd$ states via ejection of high-energy electrons along the common laser polarization and spectrometer axis is measured. In our initial formulation of the experiment, we assume that these quantities are identical. Nevertheless, in principle, there could be differences between the two. First, configuration interaction in the $4pNd$ or $4dNd$ channels could lead to a time-dependent variation in the angular and energy distribution of electrons ejected from the $4dNd$ states [13]. Second, because the energy-dependent transition moment between the $4pNd$ and $4dNd$ configurations changes in response to the time-dependent field of the moving Rydberg wave packet [18], the $4pNd$-$4dNd$ excitation probability could be time dependent.

Our reasons for neglecting these potential complications are as follows. First, since the *time-integrated* yield is measured, we expect that any temporal variation in the angular or energy distribution of electrons ejected from the $4dNd$ wave packet will average out over its lifetime. Second, for the high-lying Rydberg states investigated here, the $4p_{3/2}nd$ series is degenerate with the $4p_{1/2}\epsilon\ell$ continua and is energetically isolated from any other perturbing bound channels. Therefore, configuration interaction does not play a role, and the initial state in the second ICE is always a superposition of $4p_{3/2}nd$ levels. Third, because the bandwidth of ICE2 is roughly ten times greater than the width of the $4dnd$ excitation profiles, small changes in the ICE line shape [18] should not affect the total $4pNd-4dNd$ excitation probability. However, despite the apparent legitimacy of these arguments, the fact remains that there is a clear difference between the rate parameters required to fit the decay curves obtained for initial $4snd$ eigenstates as opposed to radial wave packets.

TABLE I. $LS$ $K$ matrices at energy $=-0.321\,646$ a.u. [38].

| $^1P_0$ | $4snp$ | $3dnp$ | $3dnf$ | $4pns$ | $4pnd$ |
|---|---|---|---|---|---|
| $4snp$ | −0.11385 | 0.12953 | 0.17339 | −0.97642 | −0.25674 |
| $3dnp$ | 0.12953 | −0.78481 | 0.33251 | −1.6152 | −0.098125 |
| $3dnf$ | 0.17339 | 0.33251 | −0.39437 | −0.26045 | 0.72937 |
| $4pns$ | −0.97642 | −1.6152 | −0.26045 | −0.97277 | 1.1504 |
| $4pnd$ | −0.25674 | −0.098125 | 0.72937 | 1.1504 | −0.53812 |

| $^3P_0$ | $4snp$ | $3dnp$ | $3dnf$ | $4pns$ | $4pnd$ |
|---|---|---|---|---|---|
| $4snp$ | −0.33937 | 0.34323 | −0.09064 | −0.56855 | 0.29591 |
| $3dnp$ | 0.34323 | −0.45516 | 0.002109 | −1.5611 | −0.59313 |
| $3dnf$ | −0.090640 | 0.002109 | −0.22377 | −0.22375 | 0.62998 |
| $4pns$ | −0.56855 | −1.5611 | −0.22375 | 3.6092 | 0.44188 |
| $4pnd$ | 0.29591 | −0.59313 | 0.62998 | 0.44188 | −0.63770 |

| $^3D_0$ | $3dnp$ | $3dnf$ | $4pnd$ |
|---|---|---|---|
| $3dnp$ | −0.82238 | 0.031903 | 0.46628 |
| $3dnf$ | 0.031903 | −0.039409 | 0.40638 |
| $4pnd$ | 0.46628 | 0.40638 | −0.32777 |

| $^1F_0$ | $4snf$ | $3dnp$ | $3dnf$ | $4pnd$ | $4png$ |
|---|---|---|---|---|---|
| $4snf$ | 0.22830 | 0.32957 | −0.14201 | 0.37450 | −0.062271 |
| $3dnp$ | 0.32957 | −1.5613 | −0.064441 | 1.1987 | −0.095575 |
| $3dnf$ | −0.14201 | −0.064441 | −0.022135 | 0.53045 | −0.059457 |
| $4pnd$ | 0.37450 | 1.1987 | 0.53045 | −1.6966 | 0.14259 |
| $4png$ | −0.062271 | −0.095575 | −0.059457 | 0.14259 | −0.12945 |

| $^3F_0$ | $4snf$ | $3dnp$ | $3dnf$ | $4pnd$ | $4png$ |
|---|---|---|---|---|---|
| $4snf$ | 0.34515 | −0.18247 | −0.063689 | 0.24536 | −0.041226 |
| $3dnp$ | −0.18247 | −0.61997 | −0.075997 | −0.044269 | −0.0085487 |
| $3dnf$ | −0.063689 | −0.075997 | 0.12687 | 0.26260 | −0.019838 |
| $4pnd$ | 0.24536 | −0.044269 | 0.26260 | −0.21046 | −0.040918 |
| $4png$ | −0.041226 | −0.0085487 | −0.019838 | −0.040918 | −0.10687 |

| $^3G_0$ | $3dnf$ | $4png$ |
|---|---|---|
| $3dnf$ | 0.090996 | −0.0030878 |
| $4png$ | −0.0030878 | 0.14447 |

## V. *K*-MATRIX ASSISTED, 28-CHANNEL QDT ANALYSIS

Fortunately, *ab initio K* matrices have been calculated for the $4pnd$ $J=1,3$ system [38], and numerical MQDT simulations based on these matrices have been in excellent agreement with previous experimental results [13] (see Table I). Because these calculations have no adjustable parameters, we should be able to determine which (if either) of the two-channel QDT fits provides a better approximation of reality. Any disagreement between the data and the 28-channel MQDT simulation will indicate that either (i) the assumptions presented in the preceding paragraph are invalid; or (ii) some other effect that we have failed to identify is responsible for the difference between the effective decay rate of the shock- and radial wave packets.

The numerical simulation is based on $J=1,3$ $K$ matrices calculated in $LS$ coupling for calcium [38]. The $J=1$ matrices include 13 bound and continuum channels while there are 15 channels in the $J=3$ matrices. Both show a slight energy dependence. The matrices are rotated into the $jj$-coupled basis and the energy-dependent ICE1 transition moment into each $jj$-coupled continuum channel is then calculated using the MQDT formalism of Cooke and Cromer [20].

For $J=1$, the transformation matrix $V_1$ that rotates the $LS$-coupled states to the $jj$-coupled form is

$$
\begin{pmatrix}
4s_{1/2}np_{1/2} \\ 4s_{1/2}np_{3/2} \\ 3d_{3/2}np_{1/2} \\ 3d_{3/2}np_{3/2} \\ 3d_{5/2}np_{3/2} \\ 3d_{3/2}nf_{5/2} \\ 3d_{5/2}nf_{5/2} \\ 3d_{5/2}nf_{7/2} \\ 4p_{1/2}ns_{1/2} \\ 4p_{3/2}ns_{1/2} \\ 4p_{1/2}nd_{3/2} \\ 4p_{3/2}nd_{3/2} \\ 4p_{3/2}nd_{5/2}
\end{pmatrix}
=
\begin{pmatrix}
\frac{1}{\sqrt{3}} & \sqrt{\frac{2}{3}} & 0 & 0 & 0 & 0 & 0 & 0 & 0 & 0 & 0 & 0 & 0 \\
0 & 0 & \frac{1}{\sqrt{3}} & \frac{-1}{\sqrt{15}} & \sqrt{\frac{3}{5}} & 0 & 0 & 0 & 0 & 0 & 0 & 0 & 0 \\
0 & 0 & 0 & 0 & 0 & \sqrt{\frac{2}{5}} & \frac{1}{\sqrt{35}} & \frac{2}{\sqrt{7}} & 0 & 0 & 0 & 0 & 0 \\
0 & 0 & 0 & 0 & 0 & 0 & 0 & 0 & \frac{-1}{\sqrt{3}} & \sqrt{\frac{2}{3}} & 0 & 0 & 0 \\
0 & 0 & 0 & 0 & 0 & 0 & 0 & 0 & 0 & 0 & \frac{1}{\sqrt{3}} & \frac{1}{\sqrt{15}} & \sqrt{\frac{3}{5}} \\
\sqrt{\frac{2}{3}} & \frac{-1}{\sqrt{3}} & 0 & 0 & 0 & 0 & 0 & 0 & 0 & 0 & 0 & 0 & 0 \\
0 & 0 & \frac{-1}{\sqrt{6}} & \sqrt{\frac{8}{15}} & \sqrt{\frac{3}{10}} & 0 & 0 & 0 & 0 & 0 & 0 & 0 & 0 \\
0 & 0 & 0 & 0 & 0 & \frac{1}{\sqrt{5}} & \sqrt{\frac{18}{35}} & \frac{-\sqrt{2}}{\sqrt{7}} & 0 & 0 & 0 & 0 & 0 \\
0 & 0 & 0 & 0 & 0 & 0 & 0 & 0 & \sqrt{\frac{2}{3}} & \frac{1}{\sqrt{3}} & 0 & 0 & 0 \\
0 & 0 & 0 & 0 & 0 & 0 & 0 & 0 & 0 & 0 & \frac{1}{\sqrt{6}} & \sqrt{\frac{8}{15}} & \frac{-\sqrt{3}}{\sqrt{10}} \\
0 & 0 & \frac{1}{\sqrt{2}} & \sqrt{\frac{2}{5}} & \frac{-1}{\sqrt{10}} & 0 & 0 & 0 & 0 & 0 & 0 & 0 & 0 \\
0 & 0 & 0 & 0 & 0 & \sqrt{\frac{2}{5}} & \frac{-4}{\sqrt{35}} & \frac{-1}{\sqrt{7}} & 0 & 0 & 0 & 0 & 0 \\
0 & 0 & 0 & 0 & 0 & 0 & 0 & 0 & 0 & 0 & \frac{1}{\sqrt{2}} & \frac{-\sqrt{2}}{\sqrt{5}} & \frac{-1}{\sqrt{10}}
\end{pmatrix}
\begin{pmatrix}
4snp\,^1P \\ 3dnp\,^1P \\ 3dnf\,^1P \\ 4pns\,^1P \\ 4pnd\,^1P \\ 4snp\,^3P \\ 3dnp\,^3P \\ 3dnf\,^3P \\ 4pns\,^3P \\ 4pnd\,^3P \\ 3dnp\,^3D \\ 3dnf\,^3D \\ 4pnd\,^3D
\end{pmatrix}
$$

and the transformation matrix $\underline{V_3}$ for $J=3$ is

$$
\begin{pmatrix}
4s_{1/2}nf_{5/2} \\ 4s_{1/2}nf_{7/2} \\ 3d_{5/2}np_{1/2} \\ 3d_{3/2}np_{3/2} \\ 3d_{5/2}np_{3/2} \\ 3d_{3/2}nf_{5/2} \\ 3d_{5/2}nf_{5/2} \\ 3d_{3/2}nf_{7/2} \\ 3d_{5/2}nf_{7/2} \\ 4p_{3/2}nd_{3/2} \\ 4p_{1/2}nd_{5/2} \\ 4p_{3/2}nd_{5/2} \\ 4p_{1/2}ng_{7/2} \\ 4p_{3/2}ng_{7/2} \\ 4p_{3/2}ng_{9/2}
\end{pmatrix}
=
\begin{pmatrix}
0 & 0 & \frac{-\sqrt{2}}{3} & \frac{\sqrt{2}}{\sqrt{30}} & \frac{4\sqrt{2}}{9\sqrt{5}} & 0 & 0 & 0 & 0 & 0 & 0 & 0 & 0 & 0 & 0 \\
0 & 0 & 0 & 0 & 0 & \frac{-4}{7\sqrt{10}} & \frac{-3\sqrt{3}}{7\sqrt{5}} & \frac{3\sqrt{2}}{7} & \frac{2\sqrt{6}}{7} & 0 & 0 & 0 & 0 & 0 & 0 \\
0 & 0 & 0 & 0 & 0 & 0 & 0 & 0 & 0 & \frac{-\sqrt{2}}{\sqrt{30}} & \frac{\sqrt{2}}{3} & \frac{4\sqrt{2}}{9\sqrt{5}} & 0 & 0 & 0 \\
\frac{\sqrt{3}}{\sqrt{7}} & \frac{2}{\sqrt{7}} & 0 & 0 & 0 & 0 & 0 & 0 & 0 & 0 & 0 & 0 & 0 & 0 & 0 \\
0 & 0 & \frac{1}{\sqrt{3}} & \frac{-\sqrt{2}}{\sqrt{5}} & \frac{2}{\sqrt{15}} & 0 & 0 & 0 & 0 & 0 & 0 & 0 & 0 & 0 & 0 \\
0 & 0 & 0 & 0 & 0 & \frac{3}{\sqrt{35}} & \frac{\sqrt{6}}{\sqrt{35}} & \frac{-1}{\sqrt{7}} & \frac{\sqrt{3}}{\sqrt{7}} & 0 & 0 & 0 & 0 & 0 & 0 \\
0 & 0 & 0 & 0 & 0 & 0 & 0 & 0 & 0 & \frac{\sqrt{2}}{\sqrt{5}} & \frac{-1}{\sqrt{3}} & \frac{2}{\sqrt{15}} & 0 & 0 & 0 \\
0 & 0 & 0 & 0 & 0 & 0 & 0 & 0 & 0 & 0 & 0 & 0 & \frac{1}{\sqrt{3}} & \frac{1}{3} & \frac{\sqrt{5}}{3} \\
\frac{2}{\sqrt{7}} & \frac{-\sqrt{3}}{\sqrt{7}} & 0 & 0 & 0 & 0 & 0 & 0 & 0 & 0 & 0 & 0 & 0 & 0 & 0 \\
0 & 0 & \frac{2}{3} & \frac{\sqrt{8}}{\sqrt{15}} & \frac{1}{3\sqrt{5}} & 0 & 0 & 0 & 0 & 0 & 0 & 0 & 0 & 0 & 0 \\
0 & 0 & 0 & 0 & 0 & \frac{\sqrt{3}}{2\sqrt{35}} & \frac{3\sqrt{2}}{\sqrt{35}} & \frac{\sqrt{3}}{\sqrt{7}} & \frac{-1}{2\sqrt{7}} & 0 & 0 & 0 & 0 & 0 & 0 \\
0 & 0 & 0 & 0 & 0 & 0 & 0 & 0 & 0 & \frac{\sqrt{8}}{\sqrt{15}} & \frac{2}{3} & \frac{-1}{3\sqrt{5}} & 0 & 0 & 0 \\
0 & 0 & 0 & 0 & 0 & 0 & 0 & 0 & 0 & 0 & 0 & 0 & \frac{1}{2} & \frac{1}{\sqrt{3}} & \frac{-\sqrt{5}}{2\sqrt{3}} \\
0 & 0 & 0 & 0 & 0 & \frac{3\sqrt{15}}{14} & \frac{-\sqrt{10}}{7} & \frac{\sqrt{3}}{7} & \frac{-3}{14} & 0 & 0 & 0 & 0 & 0 & 0 \\
0 & 0 & 0 & 0 & 0 & 0 & 0 & 0 & 0 & 0 & 0 & 0 & \frac{\sqrt{5}}{2\sqrt{3}} & \frac{-\sqrt{5}}{3} & \frac{-1}{6}
\end{pmatrix}
\begin{pmatrix}
3dnp\,^3D \\ 3dnf\,^3D \\ 4pnd\,^3D \\ 4snf\,^1F \\ 3dnp\,^1F \\ 3dnf\,^1F \\ 4pnd\,^1F \\ 4png\,^1F \\ 4snf\,^3F \\ 3dnp\,^3F \\ 3dnf\,^3F \\ 4pnd\,^3F \\ 4png\,^3F \\ 3dnf\,^3G \\ 4png\,^3G
\end{pmatrix}
$$

Using these transformation matrices, the $jj$-coupled $K$ matrices are

$$\underline{K}^{jj}=\underline{V}^{T}\underline{K}^{LS}\underline{V}. \tag{4}$$

The $K$ matrices can be equated with the reaction matrices in the standard Cooke and Cromer formalism $K^{jj}=R$. The energy-dependent spectral amplitudes of the bound and continuum channels are determined, using

$$[\underline{K}+\tan(\pi\boldsymbol{\nu})]\mathbf{a}=0, \tag{5}$$

where $a_i=\cos(\pi\nu_i)A_i$, and the $A_i$ are the spectral amplitudes we seek [24]. In general, for each value of J, $n_b$ bound and $n_c$ continuum channels contribute to the spectrum. As discussed by Cooke and Cromer, it is convenient to split the $K$ matrix into blocks corresponding to the bound and continuum parts of the matrix

$$\begin{pmatrix}[\underline{\mathbf{K}}+\tan(\pi\boldsymbol{\nu})]_{bb} & \underline{\mathbf{K}}_{bc}\\ \underline{\mathbf{K}}_{cb} & [\underline{\mathbf{K}}+\tan(\pi\boldsymbol{\nu})]_{cc}\end{pmatrix}\begin{pmatrix}\mathbf{a}_b\\ \mathbf{a}_c\end{pmatrix}=\mathbf{0}, \tag{6}$$

where $\mathbf{a}_b$ and $\mathbf{a}_c$ are column vectors with $n_b$ and $n_c$ components, respectively. This equation has $n_c$ independent solutions and, therefore, Eq. (5) reduces to an $n_c$ dimensional eigenvalue problem,

$$\{\underline{\mathbf{K}}_{cb}[\underline{\mathbf{K}}+\tan(\pi\boldsymbol{\nu})]_{bb}^{-1}\underline{\mathbf{K}}_{bc}-\underline{\mathbf{K}}_{cc}\}\mathbf{a}_c=\boldsymbol{\epsilon}_j\mathbf{a}_c, \tag{7}$$

$$\mathbf{a}_b=-[\underline{\mathbf{K}}+\tan(\pi\boldsymbol{\nu})]_{bb}^{-1}\underline{\mathbf{K}}_{bc}\mathbf{a}_c. \tag{8}$$

The $n_c$ continuum eigenvectors $\mathbf{a}_c$ are normalized by

$$[(\boldsymbol{\epsilon}_j)^2+1]\sum_{i=1}^{n_c} a_{ci}^{\,2}=1, \tag{9}$$

since the electron ionizes into one of the possible $j=1,\ldots,n_c$ continuum channels.

The $n_c$ solutions $\mathbf{A}_b=\mathbf{a}_b\sec(\pi\boldsymbol{\nu})$ give the contributing energy-dependent amplitudes from each bound channel in the $n_c$ eigencontinua. These eigencontinua are linear superpositions of the $n_c$ $jj$-coupled continua. Because we are interested in the time-dependent emission into the $jj$-coupled channels, at each energy we rotate the $n_c$ eigenvectors, $\mathbf{A}_b$ back into the $jj$-coupled basis using the transformation

$$\underline{\boldsymbol{\alpha}'}_b=\underline{\boldsymbol{\alpha}_b}\ \underline{\boldsymbol{\alpha}_c}^{T}, \tag{10}$$

where $\underline{\boldsymbol{\alpha}'}_b$ and $\underline{\boldsymbol{\alpha}_b}$ are $n_b\times n_c$ matrices composed of the $n_c$ column vectors $\mathbf{A}'_b$ and $\mathbf{A}_b$, respectively. $\underline{\boldsymbol{\alpha}_c}$ is an $n_c\times n_c$ matrix composed of the $n_c$ eigenvectors $\mathbf{A}_c$. The energy-dependent excitation amplitude in each $jj$-coupled continuum channel $i$, for $i=1$ to $n_c$ is

$$\chi_i(\nu)=\boldsymbol{\kappa}_b\mathbf{A}'_{bi}, \tag{11}$$

where $\boldsymbol{\kappa}_b$ is a row vector whose $n_b$ elements are the angular parts of the ICE transition moment from the initial $4snd$ level(s) to the bound final-state channels. The vectors $\boldsymbol{\kappa}_b$ and the corresponding channel vectors for $J=1$ and $J=3$ are

$$\boldsymbol{\kappa}_b(J=1)=\left(0\quad 0\quad -\sqrt{\frac{2}{45}}\quad \frac{-\sqrt{2}}{15}\quad \frac{-\sqrt{2}}{5}\right)\Leftrightarrow(4p_{1/2}ns_{1/2}\quad 4p_{3/2}ns_{1/2}\quad 4p_{1/2}nd_{3/2}\quad 4p_{3/2}nd_{3/2}\quad 4p_{3/2}nd_{5/2}),$$

$$\boldsymbol{\kappa}_b(J=3)=\left(\frac{\sqrt{2}}{5}\quad \frac{-1}{\sqrt{15}}\quad \frac{2}{5\sqrt{3}}\quad 0\quad 0\quad 0\right)\Leftrightarrow(4p_{3/2}nd_{3/2}\quad 4p_{1/2}nd_{5/2}\quad 4p_{3/2}nd_{5/2}\quad 4p_{1/2}ng_{7/2}\quad 4p_{3/2}ng_{7/2}\quad 4p_{3/2}ng_{9/2}).$$

By replacing $A(\nu)$ in the original two-channel approximation [see Eq. (1)] with $\chi_i(\nu)$, the transition moment into each continuum channel is determined. Following a procedure completely analogous to the two-channel case, the time-dependent decay probability into each of the $n_c$ continuum channels is calculated from its respective transition moment. The sum of all the decay probabilities, for $J=1$ and $J=3$, is subtracted from unity to give the time-dependent bound-state survival probability for the autoionizing wave packet.

## VI. DISCUSSION

Typical results of the 28-channel calculations are shown with the data and two-channel simulations in Figs. 5 and 6. For the radial wave packets in Fig. 5, the numerical results are almost indistinguishable from each other and the data. However, there is a clear discrepancy between the shock wave packet decay data and the results of the full calculation. The $K$-matrix calculation suggests that a two-channel approximation using an effective decay rate, $\gamma=0.29$ should be sufficient to reproduce both the radial and shock wave packet data. Furthermore, the fact that the full simulation agrees so well with the radial wave packet data indicates that our assumption of direct proportionality between the measured high-energy electron yield and $4pNd$ survival probability is justified.

It is interesting that the experimental shock wave packet decay curves can be fit nearly perfectly by the two-channel model if the scaled rate parameter is reduced to $\gamma=0.21$. However, we have no physical justification for modifying the value of this parameter, nor do we currently have any explanation for the small but significant discrepancy between the measured and predicted decay curves. We do note that when a $4snd$ eigenstate is exposed to ICE1, that autoionization commences at its maximum rate as the transition is proceeding. As a result, there is some ambiguity in the normalization

of the measured survival probability curve. Conversely, in the radial wave packet experiments, the probability for finding the Rydberg electron near the nucleus is essentially zero for most delays, $T_1$. Consequently, except for those brief intervals when the wave packet is passing the nucleus during ICE1, the maximum survival probability is unity for an extended period of time and there is no ambiguity as to the proper normalization of the data curves. Our results indicate that direct time-domain measurements of autoionization decay rates may be more accurately performed using wave packet as opposed to stationary initial states.

## VII. SUMMARY

We have examined the effect of constituent-state phase-shaping on the time-dependent decay of autoionizing radial wave packets in Ca. We have demonstrated that phase control enables alteration of the decay rate of these wave packets by at least a factor of 5. The observed stair step rather than exponential decay of the atoms can be qualitatively understood using a semiclassical model and is in excellent quantitative agreement with two-channel and 28-channel QDT simulations. Analogous phase control over rovibrational wave packets in molecules might provide a mechanism for enhancing or reducing transition rates through reactive channels.

## ACKNOWLEDGMENTS

We are grateful to H. van der Hart and C. Greene for making the Ca *K* matrices available to us. This work has been supported by the Packard Foundation and the Chemical Sciences, Geosciences, and Biosciences Division, Office of Science, U.S. Department of Energy Grant No. DEFG02-00ER15053.

[1] W. S. Warren, H. Rabitz, and M. Dahleh, Science **259**, 1581 (1993); H. Rabitz, R. de Vivie-Riedle, M. Motzkus, and K. Kompa, *ibid.* **288**, 824 (2000), and references within each.

[2] R. J. Levis, G. M. Menkir, and H. Rabitz, Science **292**, 709 (2001).

[3] T. C. Weinacht, J. L. White, and P. H. Bucksbaum, J. Phys. Chem. A **103**, 10 166 (1999).

[4] H. G. Muller, P. H. Bucksbaum, D. W. Schumacher, and A. Zavriyev, J. Phys. B **23**, 2761 (1990); D. W. Schumacher, F. Weihe, H. G. Muller, and P. H. Bucksbaum, Phys. Rev. Lett. **73**, 1344 (1994).

[5] L. Zhu, V. Kleiman, X. Li, S. P. Lu, K. Trentelman, and R. J. Gordon, Science **270**, 77 (1995); L. Zhu, K. Suto, J. A. Fiss, R. Wada, T. Seideman, and R. J. Gordon, Phys. Rev. Lett. **79**, 4108 (1997); J. A. Fiss, L. Zhu, R. J. Gordon, and T. Seideman, *ibid.* **82**, 65 (1999).

[6] C. Chen, Y.-Y. Yin, and D. S. Elliott, Phys. Rev. Lett. **64**, 507 (1990); Y.-Y. Yin, C. Chen, and D. S. Elliott, *ibid.* **69**, 2353 (1992).

[7] T. Nakajima and P. Lambropoulos, Phys. Rev. Lett. **70**, 1081 (1993); O. Faucher, D. Charalambidis, C. Fotakis, J. Zhang, and P. Lambropoulos, *ibid.* **70**, 3004 (1993).

[8] F. Wang, C. Chen, and D. S. Elliott, Phys. Rev. Lett. **77**, 2416 (1996).

[9] L. G. Hanson and P. Lambropoulos, Phys. Rev. Lett. **74**, 5009 (1995); T. Nakajima, J. Zhang, and P. Lambropoulos, *ibid.* **79**, 3367 (1997).

[10] X. Chen and J. A. Yeazell, Phys. Rev. Lett. **81**, 5772 (1998).

[11] J. G. Story and H. N. Ereifej, Phys. Rev. Lett. **86**, 612 (2001).

[12] R. van Leeuwen, M. L. Bajema, and R. R. Jones, Phys. Rev. Lett. **82**, 2852 (1999).

[13] R. van Leeuwen, K. Vijayalakshmi, and R. R. Jones, Phys. Rev. A **63**, 033403 (2001).

[14] D. W. Schumacher, D. I. Duncan, R. R. Jones, and T. F. Gallager, J. Phys. B **29**, L397 (1996); D. W. Schumacher, B. J. Lyons, and T. F. Gallagher, Phys. Rev. Lett. **78**, 4359 (1997); B. J. Lyons, D. W. Schumacher, D. I. Duncan, R. R. Jones, and T. F. Gallagher, Phys. Rev. A **57**, 3712 (1998).

[15] R. R. Jones and L. D. Noordam, Adv. At., Mol., Opt. Phys. **38**, 1 (1997); L. D. Noordam and R. R. Jones, J. Mod. Opt. **44**, 2515 (1997), and references within each.

[16] G. M. Lankhuijzen and L. D. Noordam, Phys. Rev. Lett. **76**, 1784 (1996); R. R. Jones, *ibid.* **76**, 3927 (1996); T. C. Weinacht, J. Ahn, and P. H. Bucksbaum, *ibid.* **80**, 5508 (1998); J. Bromage and C. R. Stroud, Jr., *ibid.* **83**, 4963 (1999); M. B. Campbell, T. J. Bensky, and R. R. Jones, Phys. Rev. A **59**, R4117 (1999); R. R. Jones and M. B. Campbell, *ibid.* **61**, 013403 (2000).

[17] T. C. Weinacht, J. Ahn, and P. H. Bucksbaum, Nature (London) **397**, 233 (1999).

[18] R. R. Jones, Phys. Rev. A **57**, 446 (1998).

[19] K. T. Lu and U. Fano, Phys. Rev. A **2**, 81 (1970); A. Guisti-Suzor and U. Fano, J. Phys. B **17**, 215 (1984); M. J. Seaton, Rep. Prog. Phys. **46**, 167 (1983).

[20] W. E. Cooke and C. L. Cromer, Phys. Rev. A **32**, 2725 (1985).

[21] T. F. Gallagher, *Rydberg Atoms*, 1st ed. (Cambridge University Press, Cambridge, England, 1994), and references therein.

[22] T. F. Gallagher, J. Opt. Soc. Am. B **4**, 794 (1987), and references therein; W. Sandner, Comments At. Mol. Phys. **20**, 171 (1987), and references therein.

[23] C. H. Greene and M. Aymar, Phys. Rev. A **44**, 1773 (1991), and references therein.

[24] C. J. Dai, G. W. Schinn, and T. F. Gallagher, Phys. Rev. A **42**, 223 (1990); G. W. Schinn, C. J. Dai, and T. F. Gallagher, *ibid.* **43**, 2316 (1991).

[25] V. Lange, U. Eichmann, and W. Sandner, J. Phys. B **22**, L361 (1989); V. Lange, M. Aymar, U. Eichmann, and W. Sandner, *ibid.* **24**, 91 (1991).

[26] M. D. Lindsay, C. J. Dai, L. T. Cai, T. F. Gallagher, F. Robicheaux, and C. H. Greene, Phys. Rev. A **46**, 3789 (1992).

[27] M. B. Campbell, T. J. Bensky, and R. R. Jones, Phys. Rev. A **57**, 4616 (1998).

[28] H. N. Ereifej and J. G. Story, Phys. Rev. A **62**, 023404 (2000).

[29] R. van Leeuwen, M. L. Bajema, and R. R. Jones, Phys. Rev. A **61**, 022716 (2000).

[30] J. E. Thoma and R. R. Jones, Phys. Rev. Lett. **83**, 516 (1999).
[31] W. E. Cooke, T. F. Gallagher, S. A. Edelstein, and R. M. Hill, Phys. Rev. Lett. **40**, 178 (1978).
[32] R. R. Jones, C. S. Raman, D. W. Schumacher, and P. H. Bucksbaum, Phys. Rev. Lett. **71**, 2575 (1993).
[33] D. W. Schumacher, J. H. Hoogenraad, D. Pinkos, and P. H. Bucksbaum, Phys. Rev. A **52**, 4719 (1995).
[34] X. Wang and W. E. Cooke, Phys. Rev. Lett. **67**, 976 (1991); Phys. Rev. A **46**, 4347 (1992).
[35] S. A. Bhatti, C. L. Cromer, and W. E. Cooke, Phys. Rev. A **24**, 161 (1981).
[36] J. A. Armstrong, P. Esherick, and J. J. Wynne, Phys. Rev. A **15**, 180 (1977).
[37] R. R. Jones, Phys. Rev. A **58**, 2608 (1998).
[38] H. van der Hart and C. H. Greene (private communication).